Petroleum Science 23 (2026) 7399–7415

Contents lists available at ScienceDirect

Petroleum Science

journal homepage: www.keaipublishing.com/en/journals/petroleum-science

Original Paper

Fracture propagation mechanisms in shale across structural positions of complex tectonic zones under supercritical CO_2 fracturing

Zhi-Wei Wang [a], Zhong-Hu Wu [a,*], Wen-Ji-Bin Sun [b], Yu-Jun Zuo [b], Rong-Hua Zhang [a], Bo Lu [a], Jin-Yuan Liu [a]

[a] College of Civil Engineering, Guizhou University, Guiyang, 550025, Guizhou, China
[b] Mining College, Guizhou University, Guiyang, 550025, Guizhou, China

ARTICLE INFO

Article history:
Received 21 January 2026
Received in revised form
23 April 2026
Accepted 25 May 2026
Available online 30 May 2026

Edited by Meng-Jiao Zhou

Keywords:
Shale gas
SC-CO_2 fracturing
Complex tectonic zone
Fracture propagation
True triaxial experiment
In-situ stress difference

ABSTRACT

Supercritical CO_2 (SC-CO_2) fracturing has significant potential for shale gas stimulation and CO_2 geological sequestration. However, the differentiated fracture propagation mechanisms of shale from different structural positions in complex tectonic zones under SC-CO_2 fracturing remain insufficiently understood. In this study, the Wufeng–Longmaxi Formation shale from the Anchang Syncline in northern Guizhou was selected as the research object. True triaxial SC-CO_2 fracturing experiments were conducted under simulated in-situ temperature, pressure, and three-dimensional stress conditions, and CT-based three-dimensional reconstruction was combined to quantitatively analyze the breakdown pressure, fracture morphology, and spatial connectivity characteristics of shale from the core and limb. The results show that the average breakdown pressure of the core specimens is 33.17 MPa, which is higher than that of the limb specimens at 28.51 MPa, indicating that strong tectonic compression and high in-situ stress confinement significantly increase the fracture-initiation threshold. Fractures in the core mainly propagate steadily along the direction of the maximum horizontal principal stress, with relatively simple propagation paths. In contrast, fractures in the limb are more strongly controlled by natural fractures and bedding-related weak planes, making them more prone to deflection, branching, and the formation of complex fracture networks with large dip angles. Further analysis reveals that an increase in horizontal stress difference ($\Delta\sigma_h$) not only reduces breakdown pressure, but also amplifies the fracture propagation response through structural-position differences. In the core, this effect is mainly manifested by accelerated fracture initiation and penetration, whereas in the limb, it is more conducive to weak-plane activation and the formation of complex fracture networks. This study clarifies the fracture propagation behavior of SC-CO_2 fracturing in shale from different structural positions in complex tectonic zones, providing a basis for differentiated shale gas fracturing design and CO_2 sequestration evaluation.

© 2026 The Authors. Publishing services by Elsevier B.V. on behalf of KeAi Communications Co. Ltd. This is an open access article under the CC BY license (http://creativecommons.org/licenses/by/4.0/).

1. Introduction

As a low-carbon clean energy source, the efficient development of shale gas is of significant importance for adjusting China's energy structure and achieving carbon neutrality goals (Chen et al. 2024; Wu et al. 2025). Shale reservoirs are commonly characterized by low porosity and low permeability, and their economic development is highly dependent on fracturing stimulation to create high-conductivity fracture networks (Belyadi et al. 2019). At present, multi-stage multi-cluster fracturing in horizontal wells remains the dominant technology for shale gas development, and its stimulation effectiveness is closely related to the stimulated reservoir volume (Alzahabi et al. 2016; Wang et al. 2025). However, in complex tectonic zones such as northern Guizhou, water-based fracturing faces several challenges, including strong reservoir heterogeneity, well-developed bedding and natural fractures, and hydration damage of clay minerals (Dai et al. 2025; Qianli et al. 2025). Meanwhile, water-based fracturing also involves high freshwater consumption, greater implementation difficulty in water-scarce regions such as northern Guizhou, and potential

* Corresponding author
E-mail address: wuzhonghugzu@163.com (Z.-H. Wu).
Peer review under the responsibility of China University of Petroleum (Beijing).

https://doi.org/10.1016/j.petsci.2026.05.041
1995-8226/© 2026 The Authors. Publishing services by Elsevier B.V. on behalf of KeAi Communications Co. Ltd. This is an open access article under the CC BY license (http://creativecommons.org/licenses/by/4.0/).

environmental risks if flowback fluids are improperly treated (Guo et al. 2019; Da et al. 2024; Wu et al. 2024a). Under high horizontal stress difference, hydraulic fractures are more likely to propagate preferentially along the direction of the maximum horizontal principal stress, which limits effective communication with natural fractures and bedding-related weak planes and thereby affects the formation of complex fracture networks (Gong et al. 2022; Qu et al. 2022; Zhang et al. 2025).

As a waterless fracturing medium, SC-CO_2 is characterized by low viscosity, high diffusivity, and low surface tension, and can reduce water-sensitive damage while improving its penetration capacity into microfractures and bedding-related weak planes (Chen et al. 2019; Lyu et al. 2021; Hou et al. 2024). Experimental studies have shown that, compared with water-based fracturing, SC-CO_2 fracturing generally exhibits lower breakdown pressure and tends to propagate along mineral grain boundaries and natural weak planes, forming fracture networks with high roughness and complex branching (Zhang et al. 2017; Chen et al. 2021a; Zhou et al. 2025a). Meanwhile, CO_2 has a strong adsorption capacity for shale organic matter and clay minerals and can promote methane desorption through CH_4/CO_2 competitive adsorption; therefore, it has dual potential for production enhancement and CO_2 geological sequestration (Hazra et al. 2022; Wu et al. 2022). In recent years, considerable progress has been made in research on the mechanisms of SC-CO_2 fracturing, with related studies mainly focusing on breakdown pressure characteristics (Ha et al. 2018), fracture morphology characterization (Chen et al. 2021b), fluid–solid coupling effects (Chen et al. 2023; Xia et al. 2024), and operational parameter optimization (Blunt et al. 2025; Sun et al. 2025). However, most existing studies are based on relatively homogeneous shale or regularly bedded specimens from tectonically stable settings, often using small-scale samples under simplified stress conditions. Thus, they do not adequately capture how variations in structural position within complex tectonic zones influence fracture propagation under realistic geological environments.

Northern Guizhou is located in a strongly deformed belt on the outer margin of the Sichuan Basin and has experienced multiple phases of superimposed tectonic modification, forming complex fold structures represented by the Anchang Syncline (Sun et al. 2020). Affected by differences in tectonic deformation intensity, burial depth, and stress field, the syncline core and limb exhibit significant differences in in-situ stress, temperature, lithological assemblage, and the development degree of natural fractures (Wu et al. 2024b). This distinctive geological structure leads to highly heterogeneous rock mechanical behavior, fracture response, and propagation patterns across different structural positions. As a result, directly transferring fracturing theories established for stable blocks to this region entails considerable uncertainty. Currently, systematic experimental research and mechanistic understanding of the differentiated fracture propagation behavior under SC-CO_2 fracturing in such complex tectonic zones—particularly between different structural positions (core and limb)—are still lacking.

Therefore, this study uses the Anchang Syncline in northern Guizhou as a case study. Through true triaxial fracturing experiments under simulated in-situ temperature and pressure conditions, combined with three-dimensional fracture reconstruction, it systematically examines the variations in breakdown pressure, fracture geometry, propagation paths, and network complexity between core and limb shales during SC-CO_2 fracturing. This work elucidates the fracture propagation mechanisms governed by the combined effects of in-situ stress difference and structural position. The findings provide a theoretical basis and experimental support for optimizing SC-CO_2 fracturing design and enhancing the efficient development of shale gas reservoirs in complex tectonic zones. This research holds significant scientific and practical value for promoting the green development of regional shale gas resources and contributing to the achievement of carbon-neutrality goals.

2. Geological setting of the study area

As illustrated in Fig. 1, the Anchang Syncline is an inclined, broad, short-axis syncline with a relatively stable core structure and gentle stratigraphic dips (23°–45°), indicating favorable caprock sealing. Regional caprock thickness ranges from 50 to 100 m, and only small-scale reverse faults are developed. In contrast, the limbs exhibit steeper dips (up to 70° in places), poorer caprock integrity, regional caprock thickness of less than 50 m, and more extensively developed faults (Guo et al. 2022). Stress concentration in the core, attributed to “concave-focused compression” and “intense deformation”, leads to high in-situ stress contrasts and greater burial depth (approximately 2300–3000 m), accompanied by elevated formation temperatures. In contrast, the limbs display lower stress differentials resulting from “dispersed stress” and “weaker deformation”, along with relatively shallower burial depths (around 1900–2500 m) and lower formation temperatures (Ni et al. 2024; Zhou et al. 2025b). In the Wufeng-Longmaxi Formation within the syncline, high-quality shales are predominantly siliceous, containing 50%–70% brittle minerals (quartz, etc.) and 15%–45% clay minerals (primarily illite-montmorillonite interlayers and illite), exhibiting strong brittleness that provides a material foundation for fracture propagation. The average shale porosity is 3.41% (range: 0.22%–6.83%), with permeability concentrated between 0.0007×10^{-3} and 0.0083×10^{-3} μm^2, exhibiting low-pore and ultra-low-permeability characteristics (Zhang et al. 2020; Haikuan et al. 2022).

As shown in Fig. 2, pore types can be categorized into three main classes: (1) Organic pores are the most abundant, occurring within organic matter dispersed among pyrite, quartz grains, and clay minerals. They are predominantly bubble-like pores, ranging in size from 3 nm to 900 nm with diverse morphologies. (2) Inorganic pores include intragranular dissolution pores (formed by the leaching of unstable minerals such as feldspar) and intergranular pores (mainly interparticle pores between illite flakes, exhibiting good connectivity). (3) A limited number of microfractures are developed either parallel or perpendicular to bedding, with their occurrence being more pronounced in the limb.

3. Experimental design

3.1. Rock sample preparation

Rock samples for true triaxial experiments typically require cubes with side lengths of 100–300 mm. However, downhole coring is challenging and often yields cores of limited size. Therefore, samples were collected from outcrops of the Wufeng–Longmaxi Formation shales within the Anchang Syncline in northern Guizhou. As shown in Fig. 3, the brittle mineral content of the core samples (AY-H-1–4) ranges from 84% to 92%, while that of the limb samples (AY-Y-1–4) ranges from 76% to 86%. The brittle mineral content is higher in the syncline core than in the limb. Table 1 summarizes the geomechanical parameters of shale samples from different structural positions.

As shown in Fig. 4, the blocks were first cut into 200 mm × 200 mm × 200 mm cubes and then further machined into 100 mm × 100 mm × 100 mm cubes to enable post-fracturing

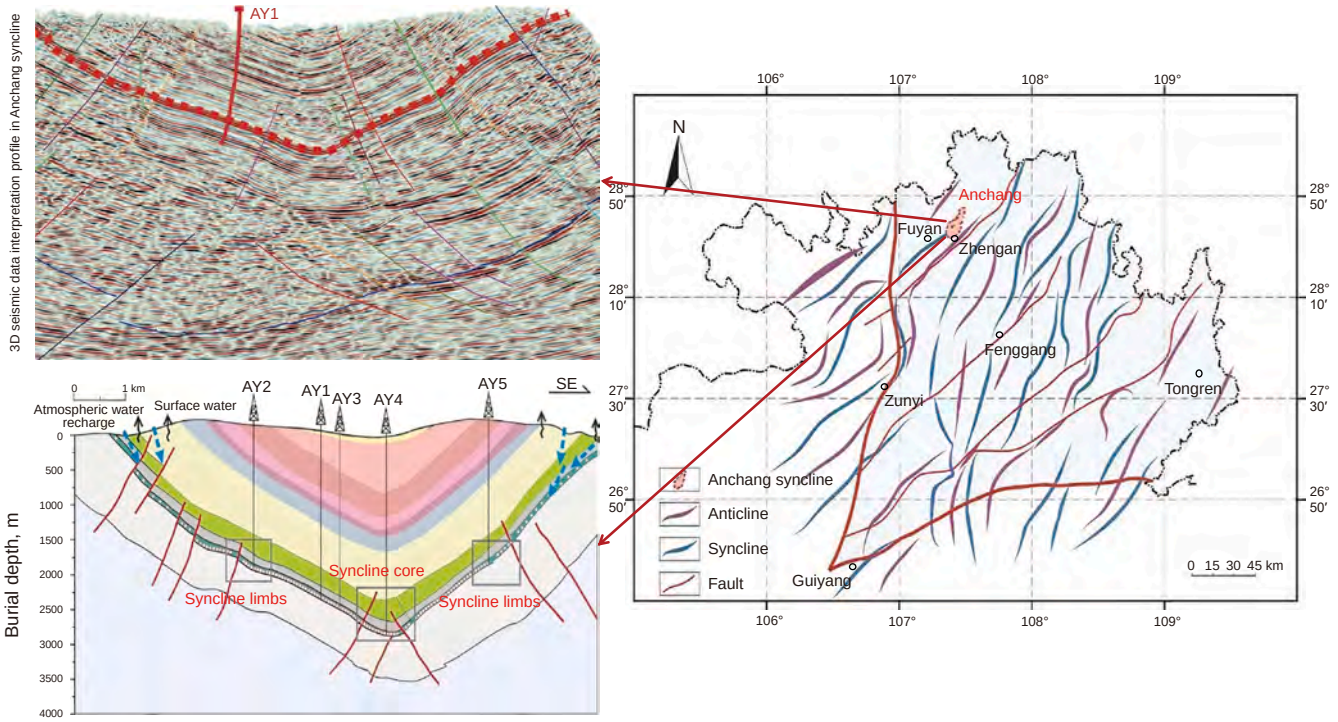


Fig. 1. Regional tectonic setting of Northern Guizhou and geological characteristics with burial depth distribution of the Anchang Syncline.

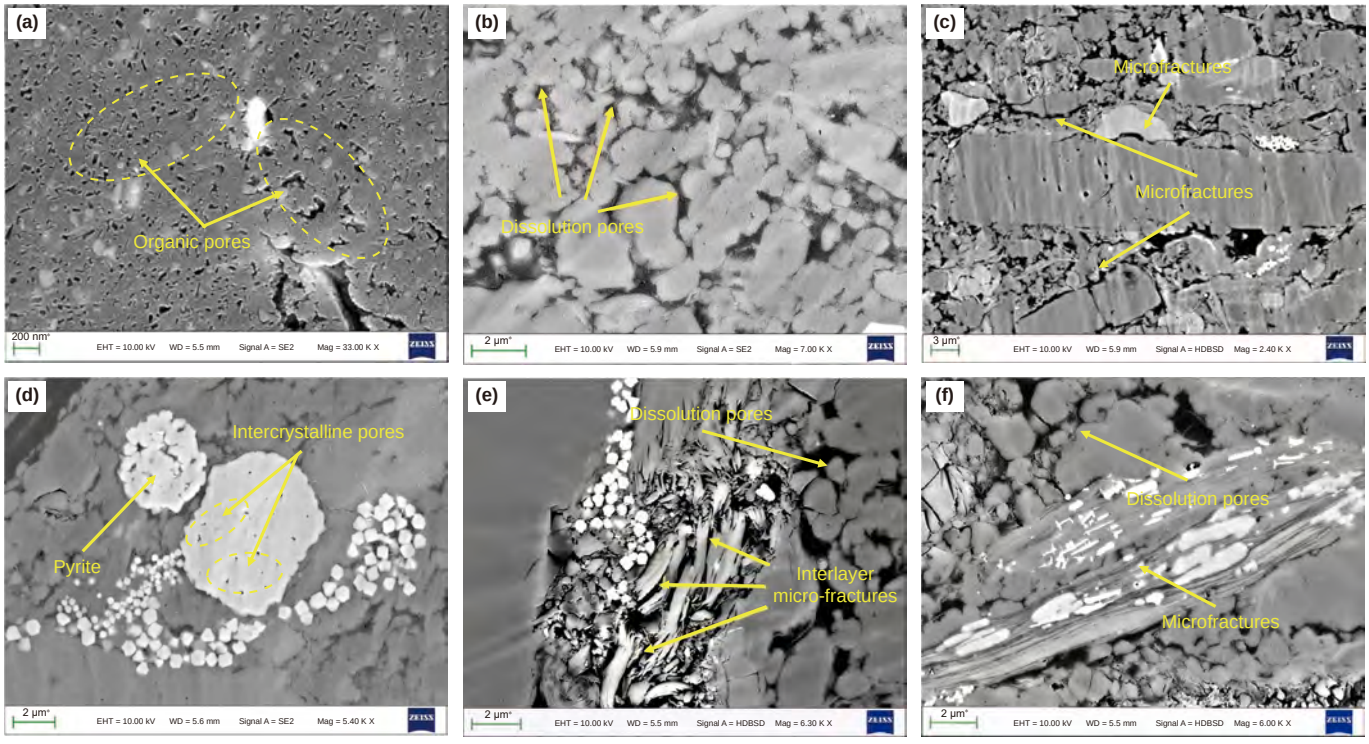


Fig. 2. Pore characteristics of the Wufeng–Longmaxi Formation shale in the study area. (**a**) Organic pores developed within organic matter; (**b**) dissolution pores distributed in mineral grains; (**c**) interlayer microfractures and microfractures developed along laminae; (**d**) intercrystalline pores associated with pyrite aggregates; (**e**) dissolution pores and interlayer microfractures; (**f**) dissolution pores and microfractures along mineral boundaries.

CT scanning of the entire specimen. A vertical wellbore 10 mm in diameter and 70 mm deep was drilled through the center of each rock cube. A metal casing was then cemented to the wellbore wall using high-strength epoxy resin. The casing had an outer diameter of 10 mm, an inner diameter of 6 mm, and a length of 50 mm, leaving a 20-mm open-hole section beneath it.

Fig. 5 shows pre-fracturing CT slices of the core (H1–H3) and limb (Y1–Y3) shale samples used in the experiments. The natural

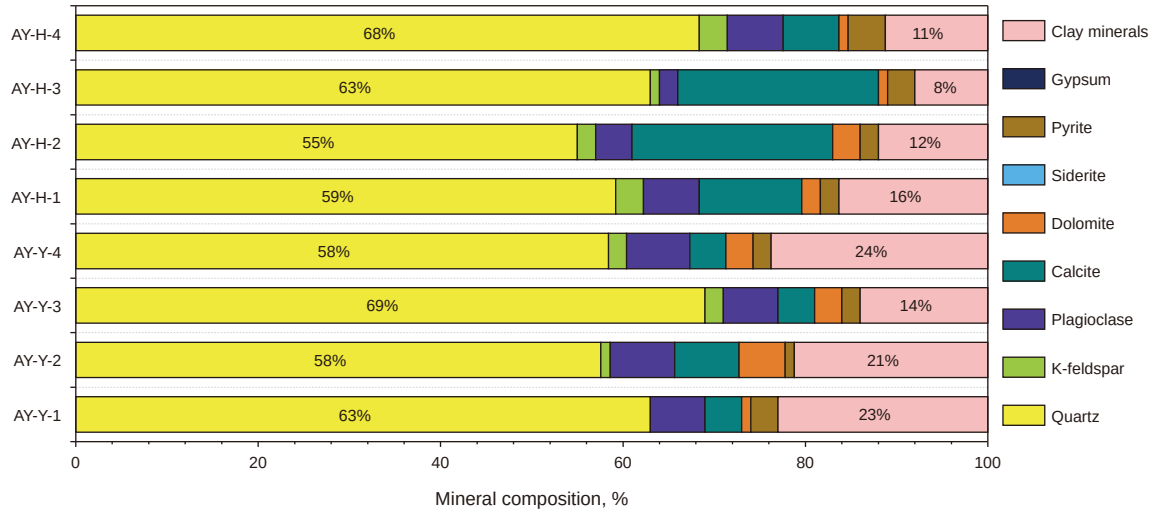


Fig. 3. Mineral composition of shale samples from different structural positions.

Table 1
Geomechanical parameters of shale samples from different structural positions.

Specimen No.	Tensile strength, MPa	Compressive strength, MPa	Poisson's ratio	Young's modulus, GPa	Natural fracture linear density, fractures/m
AY-H-1	11.81	150.28	0.228	31.41	10–20
AY-H-2	11.03	149.36	0.206	29.27	
AY-Y-1	10.80	138.12	0.195	23.54	25–40
AY-Y-2	10.08	126.41	0.182	26.38	

fracture linear density for each structural position was quantified from high-resolution pre-fracturing CT images, and the results are listed in Table 1.

3.2. True triaxial SC-CO_2 fracturing experiment

3.2.1. True triaxial fracturing system

The experiments were conducted using a self-designed true triaxial fracturing setup, as shown in Fig. 6. The system mainly comprises a fluid injection system, a triaxial loading device, a data acquisition system, and a power unit, and is suitable for cubic rock specimens with dimensions of 100 mm × 100 mm × 100 mm and 200 mm × 200 mm × 200 mm. The YS-42 hydraulic pressure system provides a maximum pressure of 100 MPa and a maximum displacement of 500 mL min^{-1}; the oil-source power system delivers a maximum pump pressure of 50 MPa; the triaxial loading device can apply a maximum axial pressure of 50 MPa; and the drying oven offers controllable temperatures from room temperature to 300 °C, incorporating temperature controllers for pipelines and intermediate vessels.

To ensure pressure-bearing safety and testing reliability during SC-CO_2 injection, the intermediate vessel, connecting pipelines, and joints in the injection system were all constructed using high-pressure-resistant components, whose pressure-bearing capacities satisfied the injection-pressure requirements of the present experiment. The injection pressure was monitored in real time by a pressure sensor installed on the high-pressure pipeline near the specimen inlet. The sensor had a measurement range of 60 MPa and an accuracy of ±0.1% FS, and the pressure signals were continuously recorded by the data acquisition system at a sampling frequency of 100 Hz.

The CT scanner used was an X5000 model from Polaris Imaging, with a scanning voltage range of 10–450 kV and a maximum resolution of about 500 nm. Based on the CT scan data, internal fractures in the post-fracturing samples were reconstructed, and the total fracture volume was calculated using the interactive thresholding function in the CT image-processing software Avizo 2019 (as shown in Fig. 7).

3.2.2. True triaxial SC-CO_2 fracturing experimental plan

The experiments were designed to simulate the fracturing process under real reservoir conditions by incorporating the actual in-situ stress differences and temperatures of the limb and core reservoirs within the Anchang Syncline in northern Guizhou, thereby providing a physical simulation of field fracturing operations. During the tests, the SC-CO_2 injection rate was kept constant at 20 mL/min. Based on actual logging data from northern Guizhou, the differential horizontal stress in the core of the Anchang Syncline ranges from about 11 MPa to 15 MPa, while in the limb it ranges from about 8 MPa to 10 MPa. Using the local geothermal gradient (2.27 °C/100 m) and surface temperature (15 °C), the formation temperatures at depth are estimated to be approximately 70 °C for the core and 50 °C for the limb. Both the experimental temperature and pressure were maintained above the supercritical point of CO_2 (31.1 °C and 7.38 MPa), ensuring that CO_2 remained in a supercritical state throughout the entire process. The experimental matrix for the true triaxial fracturing tests is presented in Table 2, where σ_V is the vertical stress, σ_H is the maximum horizontal principal stress, and σ_h is the minimum horizontal principal stress.

The fracturing tests followed the procedure outlined below: First, the rock specimen was mounted in the true triaxial loading device, ensuring the borehole was oriented vertically upward and connected to the fracturing and monitoring systems. The experimental system was then heated to the target temperatures (70 °C for the core, 50 °C for the limb) and held constant for 12 h to



Fig. 4. Preparation process of shale specimens. (**a**) Sampling location; (**b**) cutting and machining of shale blocks; (**c**) processed 100 mm × 100 mm × 100 mm cubic shale specimen.

eliminate thermal inhomogeneity. To ensure uniform stress loading, an axial stress of 2 MPa was first applied, followed by the simultaneous application of an initial confining pressure of 1 MPa in both horizontal directions. Subsequently, all three principal stresses were increased synchronously to their preset values at a rate of 0.2 MPa s^{-1}. After completing stress loading, the injection line, intermediate vessel, and wellbore were evacuated (for 0.5 h). CO_2 was then injected into the intermediate vessel; after closing the gas supply, the vessel and associated lines were preheated to 45 °C. Thereafter, the CO_2 in the intermediate vessel was driven into the rock specimen by the hydraulic pressure system while maintaining a constant injection rate of 20 mL/min, and the pressure was monitored in real time until specimen breakdown occurred. After fracturing, the confining stresses were removed and the specimen was retrieved.

4. Results and analysis

4.1. Breakdown pressure characteristics of shale from different structural positions

During the fracturing process, pressure sensors were used to monitor the pressure of the injected fluid, as shown in Fig. 8. Due to the small size of the rock samples, fracture initiation and propagation occur almost simultaneously once the ultimate strength around the wellbore is reached. Therefore, the peak value of the curve is regarded as the breakdown pressure (Meng et al. 2021).

As shown in Fig. 8, shale specimens from different structural positions exhibit pronounced differences in breakdown pressure and time to breakdown during SC-CO_2 fracturing. For the core specimens H1–H3, the breakdown pressures are 42.29, 31.29, and 25.94 MPa, respectively, with an average of 33.17 MPa. For the limb specimens Y1–Y3, the corresponding breakdown pressures are 30.41, 28.43, and 26.68 MPa, respectively, with an average of 28.51 MPa. Overall, the average breakdown pressure of the core is 4.66 MPa higher than that of the limb, representing an increase of approximately 16.35%. This indicates that fracture initiation in the core is more difficult under stronger tectonic compression and higher in-situ stress confinement.

With increasing $\Delta\sigma_h$, the breakdown pressure decreases and the time to breakdown shortens for shale at both structural positions. When $\Delta\sigma_h$ in the limb increases from 8 MPa to 10 MPa, the breakdown pressure decreases from 30.41 MPa to 26.68 MPa, corresponding to a reduction of 12.3%, while the time to breakdown shortens from 1117 s to 988 s, a reduction of 11.6%. In the core, when $\Delta\sigma_h$ increases from 11 MPa to 15 MPa, the breakdown pressure drops from 42.29 MPa to 25.94 MPa, corresponding to a

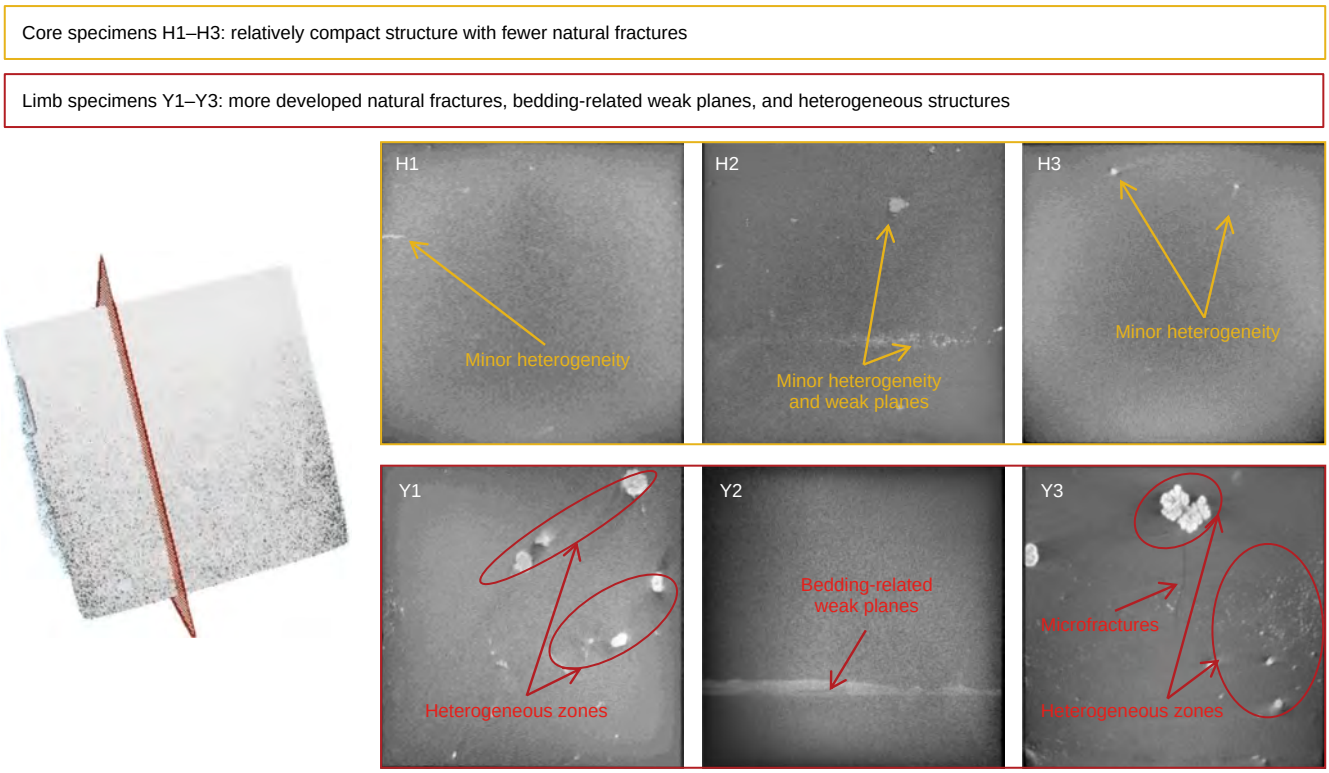


Fig. 5. Pre-fracturing CT slices of shale samples from different structural positions.

reduction of 38.7%, and the time to breakdown decreases from 1051 s to 824 s. These results indicate that, compared with the limb, an increase in $\Delta\sigma_h$ not only markedly lowers the breakdown pressure of the core, but also significantly accelerates the fracture evolution process from initiation to full penetration. This is because fracture propagation in the core is more strongly controlled by the in-situ stress field. Once the confinement in the direction of the minimum horizontal principal stress is weakened, fractures can more readily transition from local initiation to overall penetration. Consequently, the time to breakdown in the core is generally shorter than that in the limb, exhibiting a more distinct rapid-penetration characteristic. In contrast, the limb contains more well-developed natural fractures and bedding-related weak planes. During propagation, fractures are therefore more likely to undergo pressure dissipation along weak planes, as well as deflection and branching. As a result, the variations in breakdown pressure and time to breakdown with increasing $\Delta\sigma_h$ are relatively moderate, and the fracture propagation process in the limb is more likely to exhibit a progressive evolution pattern.

4.2. Fracture characteristics of shale from different structural positions

4.2.1. Morphology of main fractures

The main fracture refers to the fracture that is directly connected to the wellbore, plays a dominant role in fracture propagation during the fracturing process, and forms the primary through-going flow path. Post-fracturing samples from different structural positions of the syncline are displayed in Fig. 9. Observations of the main fracture morphology show that after SC-CO_2 fracturing, both the core and the limb developed main fractures propagating along the direction of the maximum horizontal principal stress. However, the morphological characteristics of these main fractures differ markedly due to the variation in structural position.

Therefore, to quantify the morphological differences of main fractures across structural positions, digital image analysis was applied to statistically measure the total length (L_f), dip angle relative to the maximum horizontal principal stress (θ), number of deflections (n), and maximum deflection angle (β) of the main fractures from the six experimental groups, as listed in Table 3. The total length L_f can be calculated using Eq. (1):

$$L_f = \sum_{i=1}^{n} l_i \tag{1}$$

where l_i denotes the length of an individual segment of the main fracture on the shale surface, n is the number of fracture segments, as illustrated in Fig. 10.

The average length of the main fractures in the core specimens is 55.8 cm, with relatively uniform widths typically ranging from 0.4 mm to 0.5 mm. In contrast, the limb specimens have a longer average main fracture length of 59.2 cm. Their fracture widths are non-uniform, showing distinct variations, with the widest parts reaching up to 0.8 mm. Notably, as shown in Fig. 9(a), (b), (c), the main fracture in specimen H2 is longer than those in H1 and H3. This may be attributed to the influence of the local microfracture fabric or mineral distribution in H2, which promoted greater deflection and longer extension of the main fracture. Furthermore, the θ values for the core specimens are relatively small, indicating overall gentle fracture paths and relatively stable propagation directions. The limb specimens exhibit greater variation in θ, with values for Y2 and Y3 being significantly larger than those of the core specimens. This suggests that under SC-CO_2 fracturing, fracture propagation directions in the limb change more drastically, resulting in more complex fracture morphology. As shown in Fig. 9, the main fractures in both core and limb specimens underwent multiple deflections during propagation, with this deflection

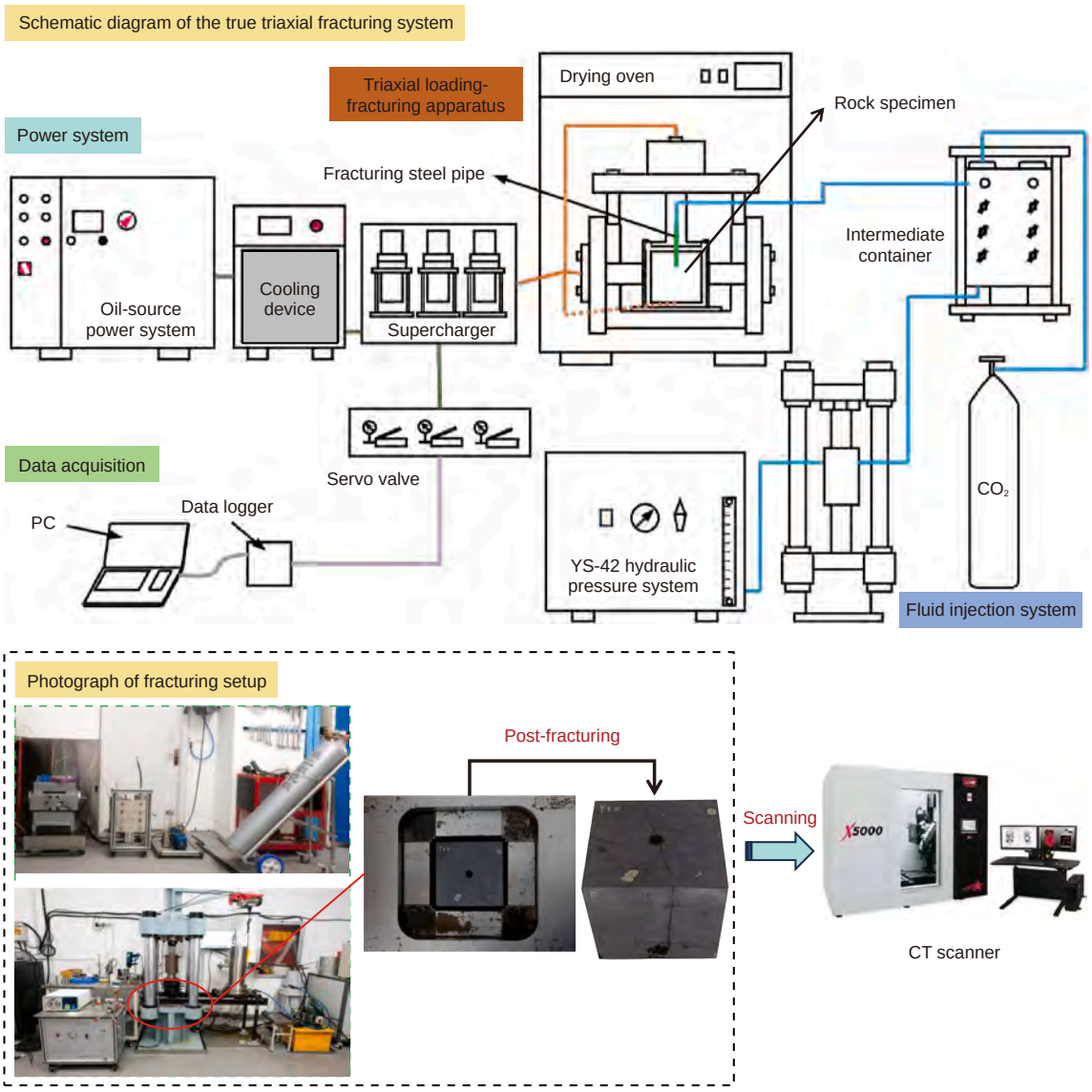


Fig. 6. True triaxial SC-CO_2 fracturing experiment flowchart.

behavior further revealing the complexity of fracture extension. The limb specimens (Y2, Y3) exhibited significantly more deflections than the core specimens. However, due to local heterogeneity, individual core specimens (e.g., H2, in the CT scan slices of Fig. 5, H2 exhibits locally developed microfracture fabrics or mineral bands within its interior compared to H1 and H3.) also developed relatively large deflection angles. It is noteworthy that while the limb specimens had a higher frequency of deflections, their maximum deflection angles were more dispersed. This indicates that fractures in the syncline limb are more prone to frequent directional changes during propagation, leading to a more complex and tortuous fracture network.

To further reveal the intrinsic mechanisms behind the morphological differences of main fractures between the core and limb shales, the transverse and vertical fracture paths on the fracture surfaces of both structural positions were compared. This provides a more fundamental explanation for why fractures in the limb are more prone to deflection and develop more branches. As shown in Fig. 11, the main fracture surfaces in the limb shale are more rugged and irregular. This difference is directly related to the initial geological conditions and failure modes of the two structural positions. When the fracture tip encounters bedding planes, mineral grain boundaries, or locally weakly cemented zones, the fracture is more prone to deflection and tends to form a mixed transgranular–intergranular fracture path (Qu et al. 2023). In contrast, the core shale has undergone stronger compaction under high in-situ stress, leading to denser mineral cementation and a more dominant stress field. Fracture propagation is primarily controlled by the direction of the regional maximum principal stress, favoring relatively straight failure. Consequently, the fracture surfaces are smoother and exhibit lower roughness.

Therefore, although the core specimens exhibit higher breakdown pressures, their main fracture morphology is relatively simple and the propagation paths are more uniform. In contrast, the limb specimens, despite having lower breakdown pressures, develop main fractures with more complex morphologies and diversified propagation directions. This contrast indicates that under identical fracturing conditions, the structural position dictates fracture initiation and propagation behavior.

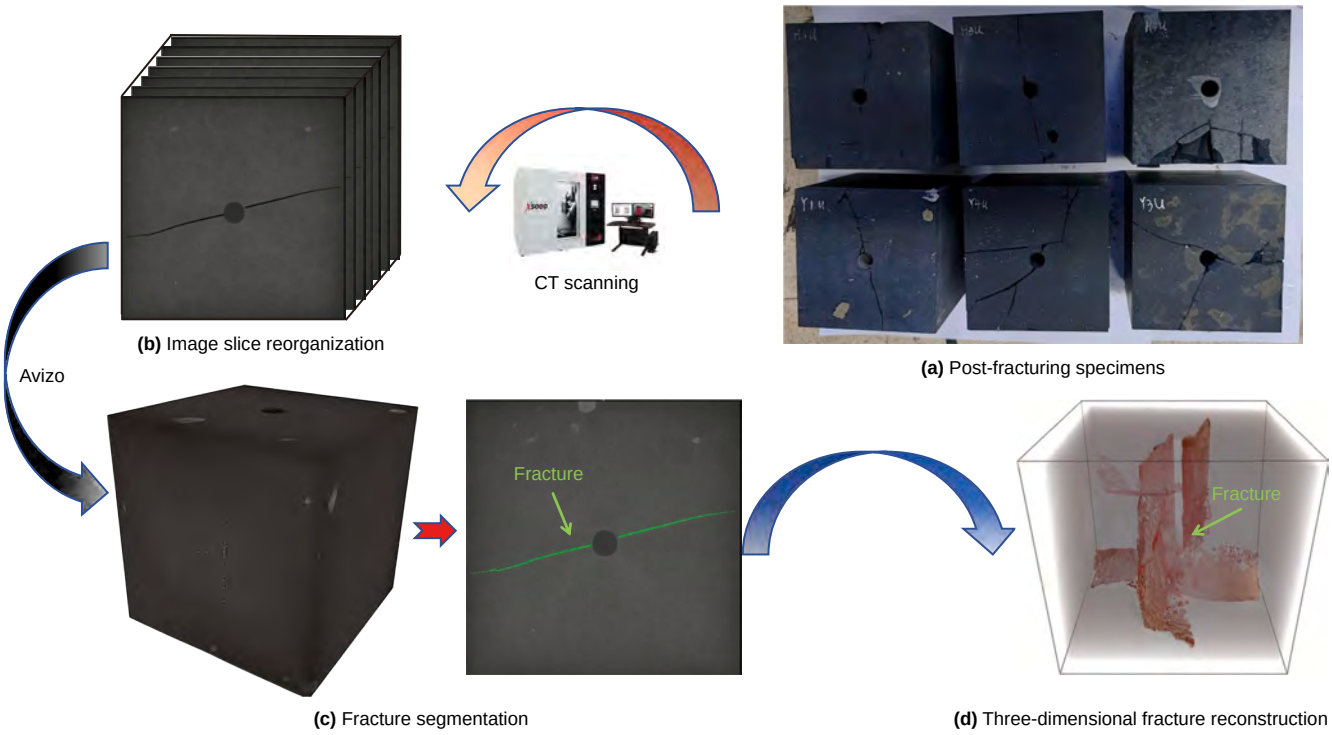


Fig. 7. Three-dimensional fracture reconstruction process within shale.

Table 2
True triaxial SC-CO_2 fracturing test scheme for shale samples from different structural positions.

Specimen No.	Fluid type	$\sigma_V/\sigma_H/\sigma_h$, MPa	Injection rate, mL/min	Temperature, °C	Breakdown pressure, MPa
H1	SC-CO_2	20/19/8	20	70	42.29
H2		20/19/6			31.29
H3		20/19/4			25.94
Y1		15/13/5	20	50	30.41
Y2		15/13/4			28.43
Y3		15/13/3			26.68

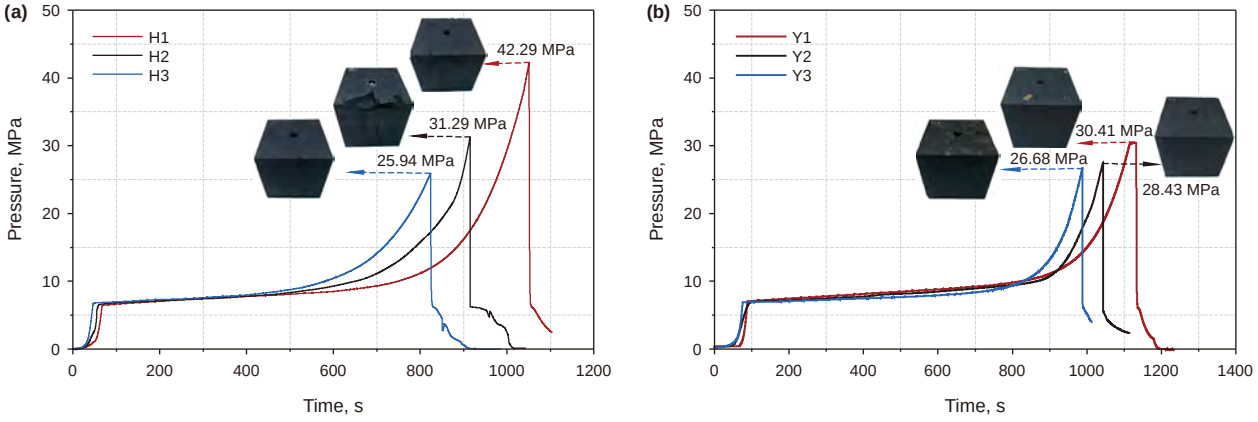


Fig. 8. Injection pressure–time curves during SC-CO_2 fracturing of shale samples from different structural positions. (**a**) Syncline core; (**b**) syncline limb.

Furthermore, in the limb characterized by a low initial $\Delta\sigma_h$, an increase in $\Delta\sigma_h$ is accompanied by growth in main fracture length (Fig. 12(a)), a significant rise in the maximum dip angle (Fig. 12(b)), an increase in the number of deflections (Fig. 12(c)), and larger deflection angles (Fig. 12(d)), showing a clear positive correlation. In contrast, in the core region under high $\Delta\sigma_h$ conditions, main fracture propagation is more strongly governed by the in-situ stress field, resulting in relatively stable paths. Consequently, the dip angles and deflection frequencies show either negative or weak correlations with $\Delta\sigma_h$.

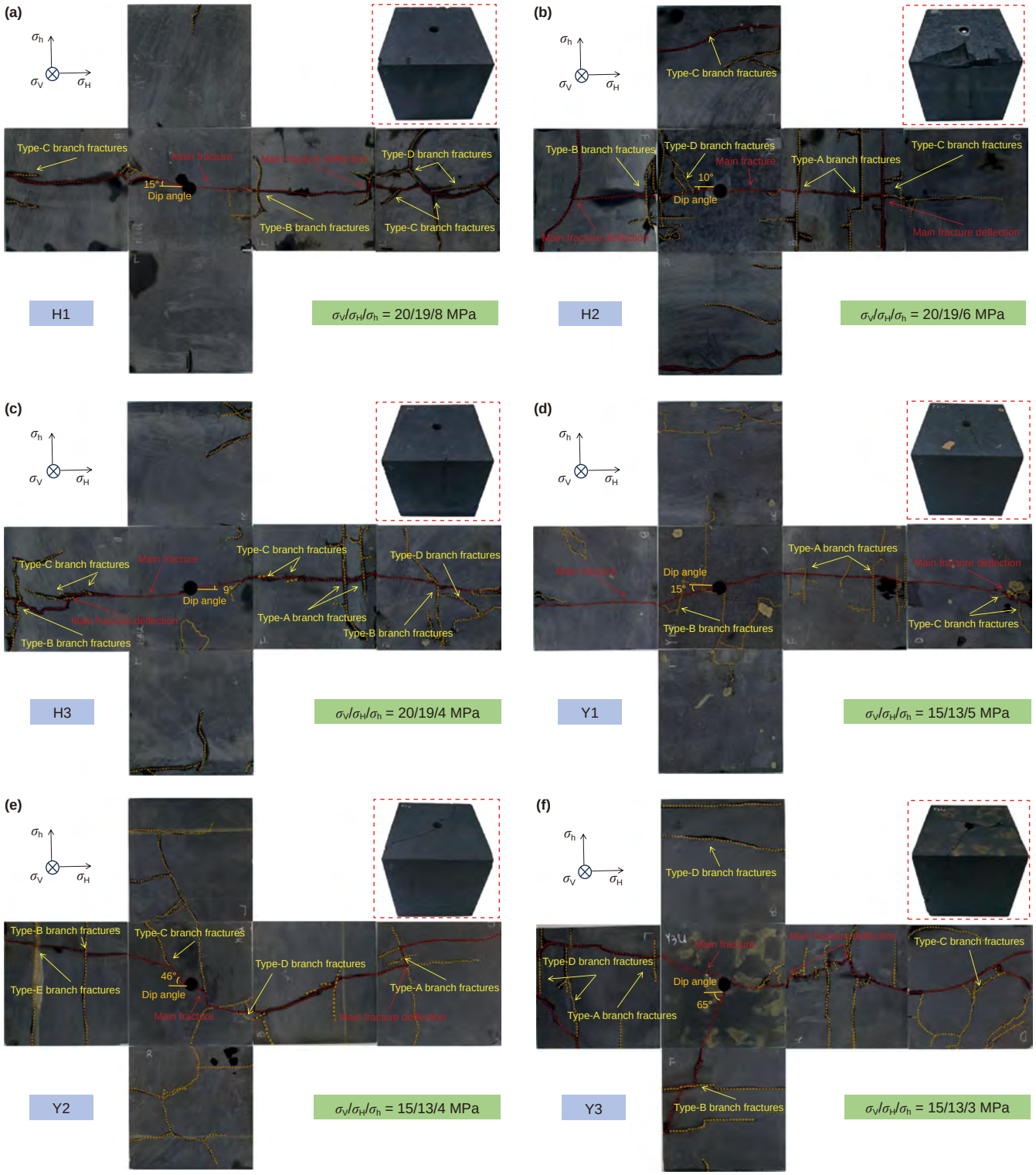


Fig. 9. Fracture propagation patterns after SC-CO_2 fracturing in shale specimens from different structural positions. (**a**) H1; (**b**) H2; (**c**) H3; (**d**) Y1; (**e**) Y2; (**f**) Y3. H1–H3 represent syncline-core samples, whereas Y1–Y3 represent syncline-limb samples.

4.2.2. Branch fracture development

Branch fractures refer to secondary fractures induced during the propagation of the main fracture by fracture-tip deflection, activation of bedding planes or natural weak planes, and local stress perturbations. As shown in Fig. 9, numerous branch fractures were induced around the main fractures in specimens from both structural positions. These branch fractures are crucial for forming complex fracture networks and enhancing reservoir permeability (Rahimi-Aghdam et al. 2019). In previous studies, researchers have frequently used the number of branch fractures to evaluate fracturing results (Wu et al. 2020; Yang et al. 2020).

Table 3
Morphological characteristics of main fractures in rock samples from different structural positions.

Specimen No.	$\sigma_V/\sigma_H/\sigma_h$, MPa	Temperature, °C	L_f, cm	θ, °	n	β, °	D_f
H1	20/19/8	70	48.4	15	7	85	1.3242
H2	20/19/6		73.3	10	4	117	1.3363
H3	20/19/4		45.7	9	4	90	1.3698
Y1	15/13/5	50	45.6	15	2	60	1.3445
Y2	15/13/4		54.3	46	8	90	1.3731
Y3	15/13/3		77.6	65	13	110	1.4152

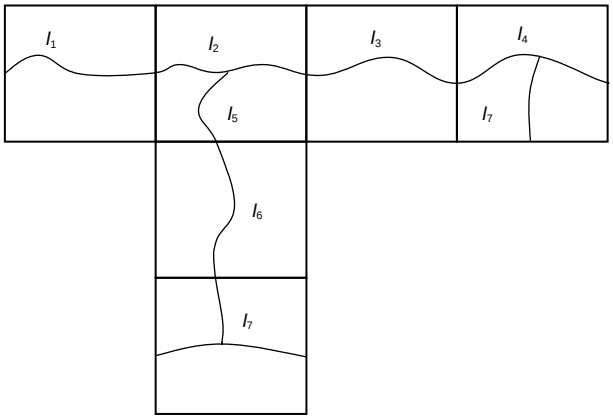


Fig. 10. Schematic diagram for calculating the length of the main fracture.

As shown in Fig. 13, the number of branch fractures in the core and limb specimens after SC-CO_2 fracturing was quantified. Based on their propagation behavior and interaction with the main fracture, the branch fractures were classified into five distinct types.

As shown in Fig. 9: Type-A: branch fractures propagate perpendicular to the main fracture, forming a "+"-shaped pattern. Type-B: branch fractures intersect the main fracture, forming an "X"-shaped pattern. Type-C: branch fractures branch off from the main fracture at an acute angle, exhibiting a "Y"-shaped pattern. Type-D: branch fractures connect directly to the main fracture. Type-E: branch fractures extend along bedding planes and cross-cut the main fracture. Statistical analysis shows that the limb specimens developed a greater number of branch fractures than the core specimens. Moreover, with increasing $\Delta\sigma_h$, the number of branch fractures in both the syncline core and limb exhibited an increasing trend, leading to the formation of more complex

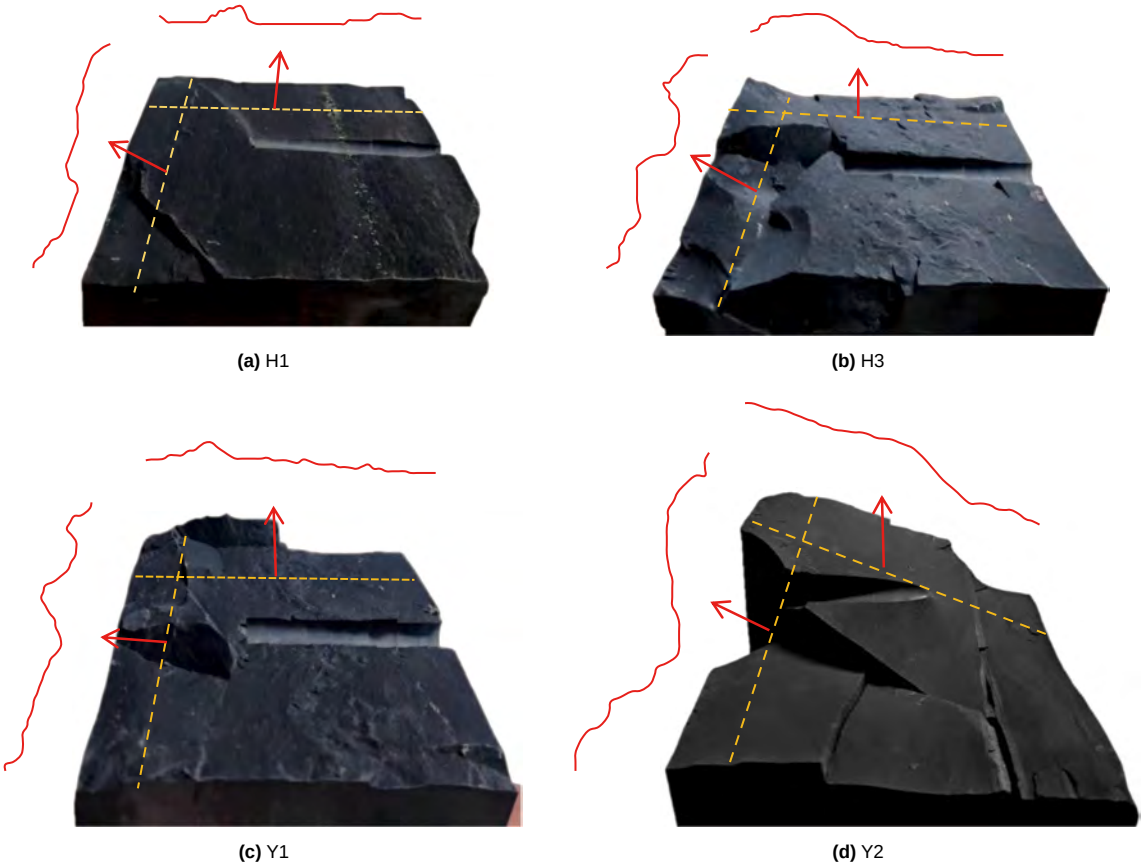


Fig. 11. Fracture trajectories on the main fracture surfaces of shale specimens from different structural positions after SC-CO_2 fracturing. (**a**), (**b**) Main fracture surfaces of syncline-core specimens; (**c**), (**d**) main fracture surfaces of syncline-limb specimens.

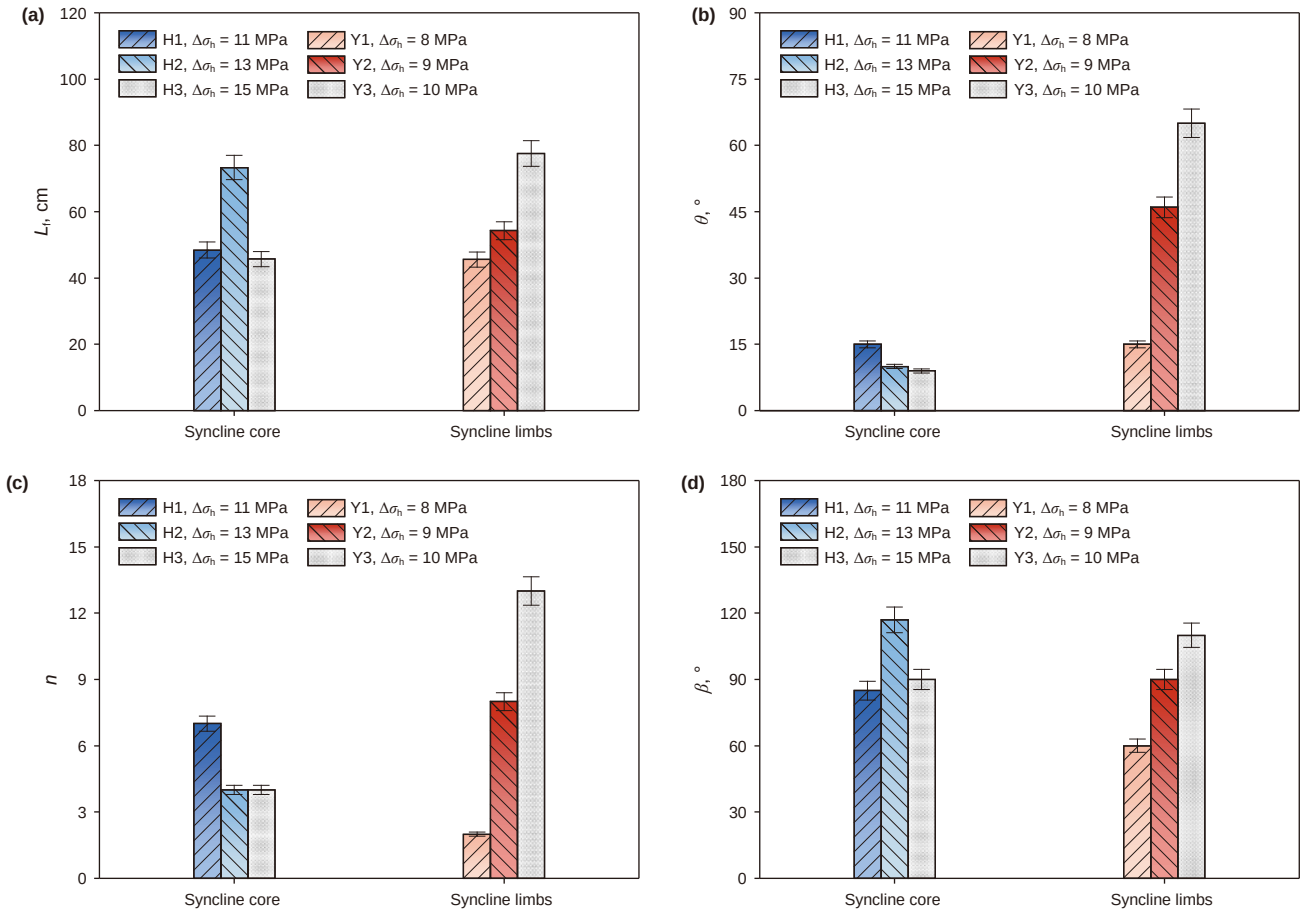


Fig. 12. Variations in main-fracture morphological parameters with $\Delta\sigma_h$ after SC-CO_2 fracturing. (**a**) L_f; (**b**) θ; (**c**) n; (**d**) β.

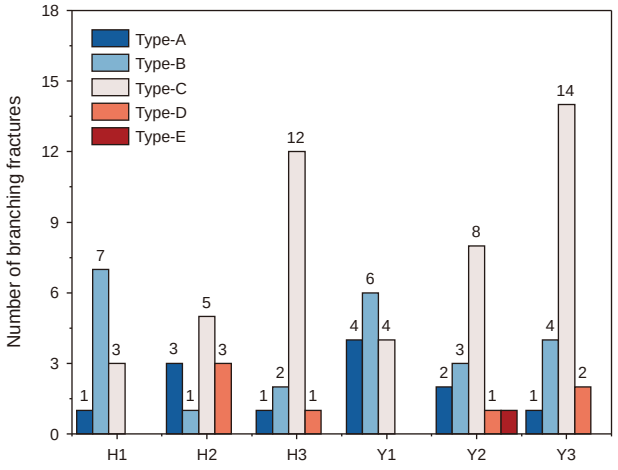


Fig. 13. Branching fracture characteristics of rock specimens from different structural positions.

fracture networks. Notably, type-E fractures were primarily observed in specimen Y2, demonstrating the ability of fractures to propagate along bedding planes and penetrate the main fracture, thereby enhancing the overall complexity of the fracture network. In contrast, branch fractures in the core tend to extend primarily in the vicinity of the main fracture, making it difficult to form a fracture network as diverse and complex as that in the limb.

4.2.3. *Fractal dimension (D_f) of fractures*

To quantitatively assess the geometric complexity of fracture networks after SC-CO_2 fracturing, this study employs the two-dimensional D_f as a key quantitative index. The D_f effectively describes the tortuosity of fracture contours, their space-filling characteristics, and the density of branching. A higher D_f value reflects greater complexity and irregularity of the fracture network (Zhou et al. 2024).

As shown in Fig. 14, based on the post-fracturing sample images, an appropriate segmentation threshold was selected to extract a binary fracture image. The D_f was then calculated using the Box-Counting method (Wang et al. 2023). By varying the square box size, variable number of overlay boxes were generated from which the fractal dimensionality of image was computed.

The D_f values of the fracture networks for different specimens were calculated using the Box-Counting method, and the results are listed in Table 3. For the core specimens H1–H3, the D_f values are 1.3242, 1.3363, and 1.3698, respectively, with an average of 1.3434. For the limb specimens Y1–Y3, the corresponding values are 1.3445, 1.3731, and 1.4152, respectively, with an average of 1.3776. Overall, the average D_f of the limb is 0.0342 higher than that of the core, quantitatively indicating that the fracture network in the limb is characterized by greater tortuosity, higher branch density, and stronger geometric complexity after fracturing. This result is consistent with the macroscopic observations that natural weak planes are more developed in the limb and that fractures are more likely to undergo deflection and branching during propagation.

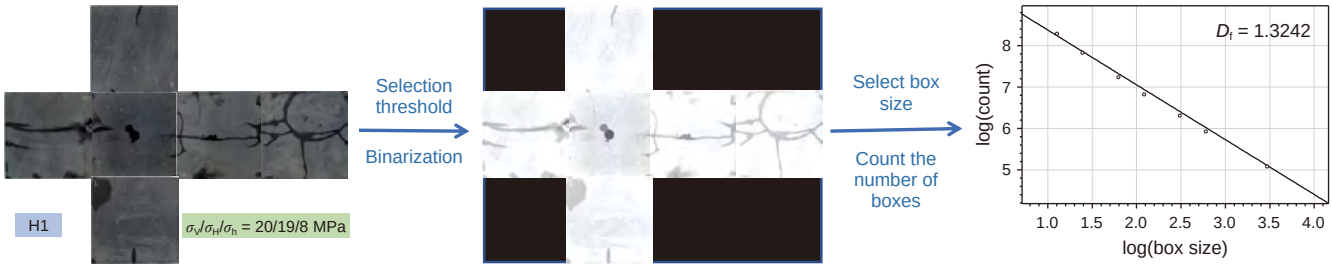


Fig. 14. Schematic diagram of the Box-Counting method for D_f calculation.

As further shown in Fig. 15, D_f increases markedly with increasing $\Delta\sigma_h$, indicating that the enhancement of $\Delta\sigma_h$ not only reduces the breakdown pressure, but also promotes the evolution of a more complex fracture network. However, comparison between the two structural positions shows that the limb, owing to its more developed natural weak planes, is more effective in transforming the effect of stress difference into fracture deflection and branch propagation, thereby forming a more intricate fracture-network structure. In contrast, although fracture complexity in the core also increases with increasing $\Delta\sigma_h$, its overall fracture propagation remains more strongly constrained by the in-situ stress field.

4.2.4. Internal connectivity of shale post-fracturing

To directly visualize the spatial distribution and connectivity of fractures in the SC-CO_2 fractured specimens, CT scanning and three-dimensional reconstruction were performed. As shown in Fig. 16, the reconstructed images reveal complex internal fracture networks with high spatial connectivity. This intricate fracture system provides favorable pathways for shale gas migration and recovery. Significant differences are observed in the post-fracturing fracture-volume characteristics of shale from different structural positions. For the core specimens, the average volumes of main fractures and branch fractures are 33421.18 mm^3 and 14795.30 mm^3, respectively, with an average total fracture volume of 48216.48 mm^3. For the limb specimens, the corresponding average volumes of main fractures and branch fractures are 35331.60 mm^3 and 28129.52 mm^3, respectively, and the average total fracture volume reaches 63461.12 mm^3, which is approximately 31.62% higher than that of the core.

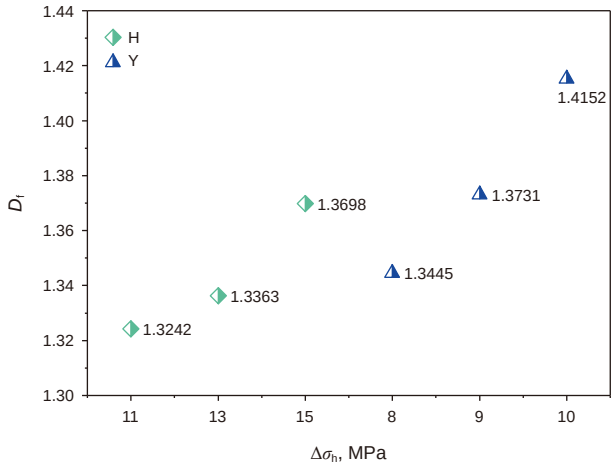


Fig. 15. Relationship between $\Delta\sigma_h$ and D_f.

As shown in Fig. 17, in terms of volumetric distribution, the fracture volume in the core is dominated by the main fractures, which account for 62.52%–76.37% of the total fracture volume, with an average proportion of 69.48%. In contrast, the contribution of branch fractures is more pronounced in the limb, where branch fractures account for 37.86%–48.70% of the total fracture volume, with an average of 43.52%. Further comparison shows that the average main-fracture volume in the limb is only about 5.72% higher than that in the core, whereas the average branch-fracture volume is increased by approximately 90.12%. This indicates that the increase in fracture volume in the limb is mainly attributed to the extensive development of branch fractures. These results demonstrate that, after SC-CO_2 fracturing, the limb is more likely to form a complex and well-connected fracture network jointly composed of main fractures and branch fractures, whereas the core remains dominated by a relatively regular fracture system controlled primarily by the main fractures. Therefore, the differences in fracture volume and its compositional characteristics between the core and the limb not only reflect the distinct fracture propagation patterns at different structural positions, but also indicate that the limb is more likely to develop a highly complex and highly connected fracture network after fracturing.

As shown in Fig. 18, scanning electron microscopy (SEM) was used to observe the surface of the main fracture in a post-fracturing specimen (H3). The surfaces of the main fracture and its branches are characterized by abundant dissolution pores and a dense network of microfractures. The presence of these pores and microfractures indicates that the fracturing process not only generated macroscopic main and branch fractures but also significantly altered the internal microstructure of the shale at the microscopic scale. This microstructural change further enhances the connectivity between the shale matrix and the fractures, creating more complex pathways for gas diffusion and migration. Moreover, the distribution of the microfractures shows a certain degree of preferred orientation, which is likely closely associated with the prevailing in-situ stress field.

5. Discussion

5.1. Differences in fracture propagation in shale across structural positions

The fracturing results indicate that shale from different structural positions of the Anchang Syncline exhibits markedly different fracture propagation patterns under SC-CO_2 fracturing. These differences are mainly governed by the combined effects of in-situ stress confinement, the development degree of natural weak planes, and the penetration capacity of the fracturing fluid. The core is characterized by greater burial depth and has long been subjected to stronger tectonic compression. As a result, the overall

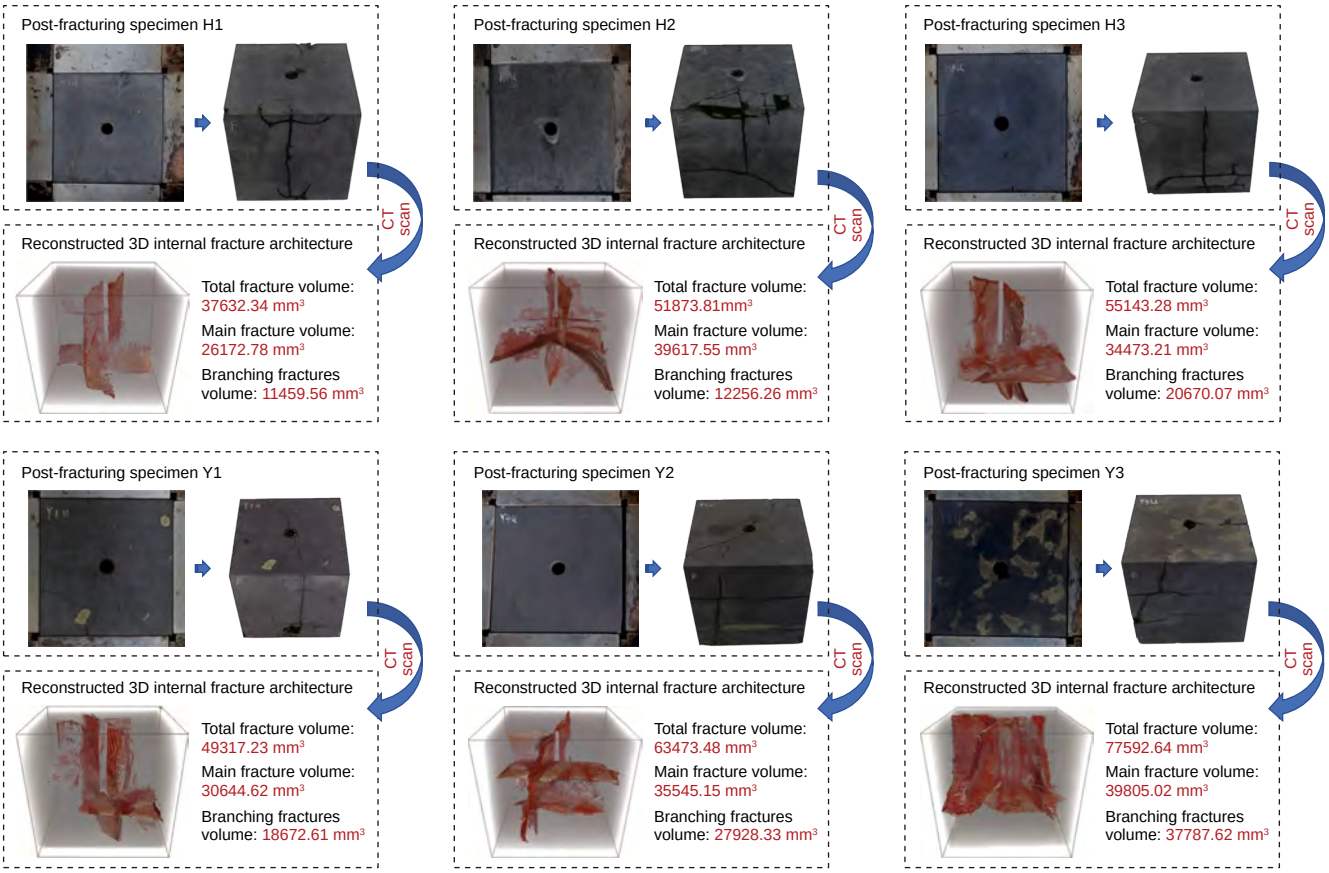


Fig. 16. 3D CT reconstruction of internal fractures in shale after fracturing.

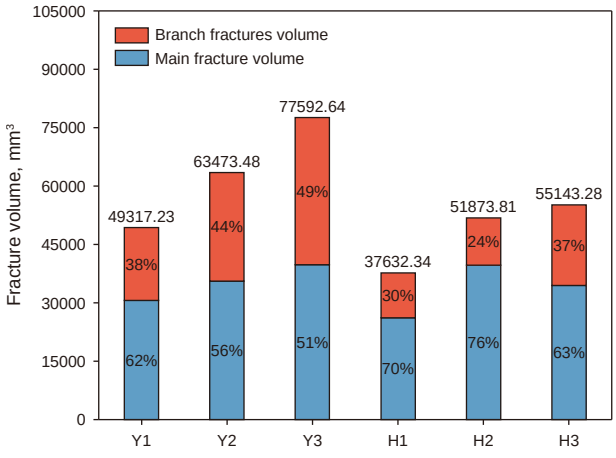


Fig. 17. Volume of main and branch fractures in shale post-fracturing.

three-dimensional stress level is higher, the rock mass is more strongly compacted, and natural fractures are more tightly closed. Therefore, fracture initiation must overcome stronger confining constraints, leading to a higher breakdown pressure. Previous studies have indicated that, under complex stress conditions, fracture initiation pressure and propagation paths are primarily controlled by the principal stress state and confining pressure level. Higher stress conditions generally increase the breakdown threshold and enhance the tendency of fractures to propagate along the principal stress direction (Saberhosseini et al. 2014; Pan et al. 2020).

In this study, the temperature difference between 50 °C and 70 °C mainly regulates the fluidity of SC-CO_2 and its ability to enter weak planes, rather than serving as the dominant explanation for thermal damage to the rock. For the core, although the higher temperature facilitates the penetration of SC-CO_2 into local microfractures, fracture propagation remains mainly governed by strong in-situ stress confinement and extends stably along the direction of the maximum horizontal principal stress. This is manifested by smaller dip angles, fewer deflections, and poorly developed branches, which is generally consistent with the understanding that fracture propagation under SC-CO_2 fracturing is controlled by stress orientation (Al Shafloot et al. 2021). In contrast, the limb is subjected to weaker stress confinement and contains more developed natural fractures and bedding-related weak planes. SC-CO_2 can therefore more readily penetrate along these weak planes and induce local fracture initiation, resulting in more pronounced deflection, branching, and multi-path propagation. This agrees with experimental observations that supercritical CO_2 can propagate along natural structural planes and promote the formation of complex fractures (Isaka et al. 2019; Gao et al. 2022).

Therefore, the difference in fracture propagation between different structural positions is not merely reflected by the magnitude of breakdown pressure, but results from the coupled effects of stress conditions, weak-plane structures, and SC-CO_2 penetration. Overall, fracture propagation in the core is more characterized by stress-dominated directional extension, whereas

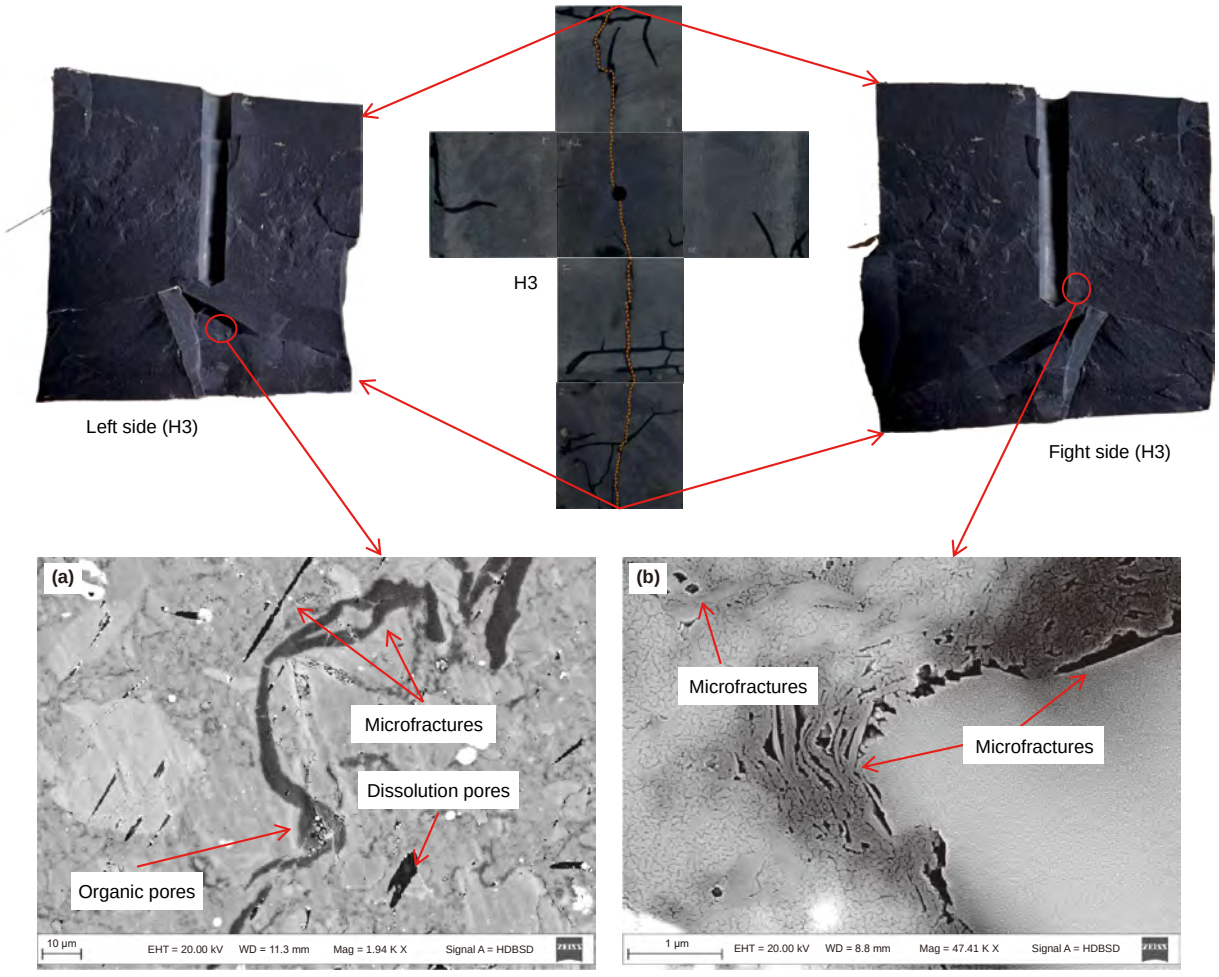


Fig. 18. Fracture connectivity in shale after SC-CO_2 fracturing.

the limb is more prone to weak-plane-activation-controlled deflection, branching, and network-like propagation.

5.2. Influence of $\Delta\sigma_h$ on fracture complexity

The experimental results indicate that increasing horizontal stress difference not only reduces the difficulty of fracture initiation and propagation, but also alters the fracture evolution mode. However, its influence differs between the core and the limb. For the core shale, increasing $\Delta\sigma_h$ mainly lowers the breakdown threshold and accelerates fracture penetration, while the overall fracture path remains controlled by the principal stress field and exhibits strong directionality. For the limb shale, in addition to reducing the initiation pressure, increasing $\Delta\sigma_h$ is more likely to couple with natural fractures, bedding planes, and local heterogeneous structures, thereby promoting fracture-tip deflection, branch proliferation, and multi-path propagation, ultimately forming a more complex fracture network.

In structurally stable and relatively homogeneous reservoirs, a higher horizontal stress difference usually strengthens the linear propagation of fractures along the direction of the maximum principal stress and suppresses branch development to some extent (Hou et al. 2018; Zhou et al. 2023). However, the shale investigated in this study has undergone strong tectonic modification and contains well-developed microfracture clusters, bedding planes, and distinct weak planes. Therefore, $\Delta\sigma_h$ in this type of reservoir does not simply act as a unidirectional stress constraint. With increasing $\Delta\sigma_h$, local stress concentration at the fracture tip is enhanced, reducing the initiation threshold of weak planes. Meanwhile, the low viscosity and high diffusivity of SC-CO_2 enable it to more readily enter these weak-plane structures, thereby promoting fracture deflection, branching, and local penetration along bedding planes, interlayers, and microfractures (Zhao et al. 2018).

Therefore, in complex tectonic zones, the effect of $\Delta\sigma_h$ is clearly dependent on structural position. In the core, it mainly promotes rapid fracture initiation and penetration under stress-dominated control. In the limb, it more readily amplifies the fracture-complexity effect associated with weak-plane activation. These results suggest that, in strongly tectonically modified shale, $\Delta\sigma_h$ not only controls the fracture propagation direction, but also jointly determines the fracture propagation mode together with the development degree of weak planes and the penetration capacity of SC-CO_2.

5.3. Differentiated fracturing and sequestration strategies based on structural position and stress field

Fig. 19 provides an integrated summary of the preceding results regarding differences in breakdown pressure, fracture fractal dimension, and fracture volume, reflecting the systematic response differences of shale from different structural positions in

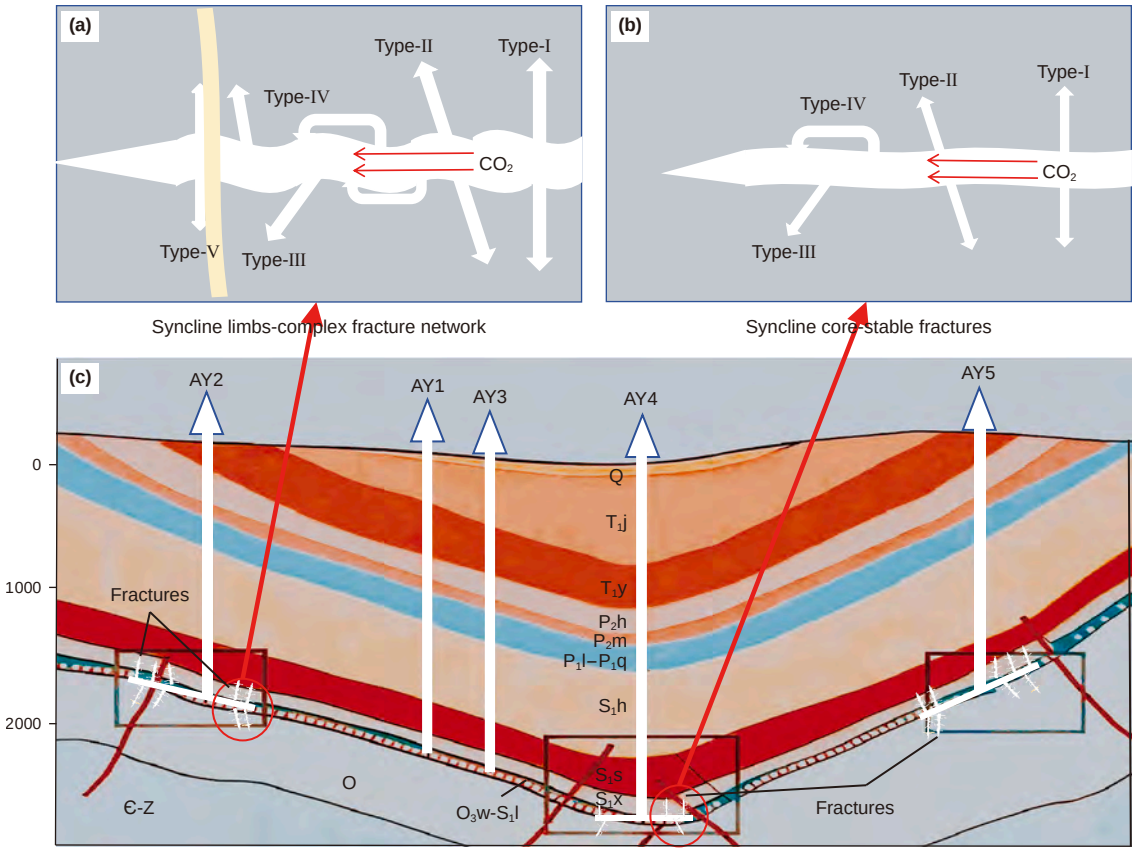


Fig. 19. Schematic diagram of near-wellbore fracture propagation at different structural positions under SC-CO_2 fracturing. (**a**) Syncline limb; (**b**) syncline core; (**c**) near-wellbore fracture propagation patterns at different structural positions.

complex tectonic zones under SC-CO_2 fracturing. In the core, fracture propagation is mainly characterized by stress-dominated directional extension. The main fractures are dominant, branch development is limited, and the fracture paths near the bottom hole are relatively concentrated. In contrast, the limb is more readily affected by natural fractures and bedding-related weak planes, exhibiting more pronounced multi-path fracture-network characteristics near the bottom hole.

Based on this understanding, the design of SC-CO_2 fracturing parameters in complex tectonic zones should not simply follow the experience derived from structurally stable regions, but should be targeted according to the differences among structural positions. The limb, with more developed natural fractures and weaker stress confinement, has inherent advantages in forming complex fracture networks and enlarging the stimulated reservoir volume. Therefore, the low viscosity, strong diffusivity, and weak-plane activation capacity of SC-CO_2 should be fully utilized. By optimizing the injection-rate schedule and stage-cluster design, fracture deflection, branching, and network connectivity can be promoted, thereby maximizing the stimulated reservoir volume.

In contrast, fracture propagation in the core is mainly controlled by the high in-situ stress difference. Although the breakdown pressure is higher, the propagation path of the main fracture is relatively stable. Therefore, the field strategy should focus on maintaining sufficient net pressure and sustained fracture-extension capacity to ensure the formation of effectively penetrating main fractures. In addition, the core is characterized by greater burial depth, stronger stress confinement, and relatively favorable structural sealing conditions, and thus has potential for CO_2 geological sequestration while enhancing reservoir permeability. However, its long-term sequestration safety still requires further verification based on caprock integrity, fault sealing capacity, and field monitoring results.

6. Conclusions

This study, taking the Anchang Syncline in northern Guizhou as a case study, reveals the differential fracture propagation mechanisms in core and limb shales under SC-CO_2 fracturing through true triaxial experimental simulations and quantitative analysis. The main conclusions are as follows.

(1) The breakdown pressure of shale from different structural positions is jointly controlled by structural position and the in-situ stress field. The average breakdown pressure of the core is 33.17 MPa, which is higher than the 28.51 MPa of the limb. Moreover, with increasing $\Delta\sigma_h$, the reduction in breakdown pressure is more pronounced in the core.

(2) Shale from different structural positions exhibits significantly different fracture propagation characteristics under SC-CO_2 fracturing. In the core, fractures mainly propagate along the direction of the maximum horizontal principal stress, with relatively regular paths. In contrast, fractures in the limb are more readily influenced by natural fractures and bedding-related weak planes, leading to deflection, branching, and multi-path propagation, and ultimately forming a more complex fracture network.

(3) The increase in $\Delta\sigma_h$ not only reduces the difficulty of fracture initiation, but also alters the mode of fracture propagation. In the core, it is mainly manifested by the acceleration of

fracture initiation and penetration. In the limb, however, it is more favorable for the involvement of weak planes in fracture propagation, thereby promoting greater fracture complexity and improved connectivity.

CRediT authorship contribution statement

Zhi-Wei Wang: Writing – review & editing, Writing – original draft, Methodology. **Zhong-Hu Wu:** Funding acquisition, Conceptualization. **Wen-Ji-Bin Sun:** Writing – review & editing, Formal analysis. **Yu-Jun Zuo:** Methodology, Investigation. **Rong-Hua Zhang:** Visualization, Supervision. **Bo Lu:** Supervision. **Jin-Yuan Liu:** Data curation.

Declaration of competing interests

The authors declare that they have no known competing financial interests or personal relationships that could have appeared to influence the work reported in this paper.

Acknowledgements

This work was supported by the National Natural Science Foundation of China Project (Project Nos. 52464004, 52264004), Guizhou Provincial High-Level Innovative Talent (Qiankexie KJLYRC-[2026]069, Guizhou Provincial Science and Technology Achievement Transformation Plan Project (Project No. Qiankehe Chengguo LH[2026]006), Guizhou Provincial Science and Technology Support Program Project (Project Nos. Qiankehe Support [2025] General 080, Qiankehe Support [2025] General 078, Qiankehe Support [2023] General 137, Qiankehe Support [2023] General 136), the Guizhou Provincial fundamental study schedule (Project No. Qiankehe Basic-ZK [2024] General 050).

References

Al Shafloot, T., Kim, T.W., Kovscek, A.R., 2021. Investigating fracture propagation characteristics in shale using sc-CO_2 and water with the aid of X-ray computed tomography. J. Nat. Gas Sci. Eng. 92 (B6), 103736. https://doi.org/10.1016/j.jngse.2020.103736.

Alzahabi, A., Berlow, N., Soliman, M.Y., et al., 2016. Multigrid fracture stimulated reservoir volume mapping coupled with a novel mathematical optimization approach to shale reservoir well and fracture design. J. Sustain. Energy Eng. 4 (3–4), 310–334. https://doi.org/10.7569/jsee.2016.629521.

Belyadi, H., Fathi, E., Belyadi, F., 2019. Hydraulic Fracturing in Unconventional Reservoirs: Theories, Operations, and Economic Analysis, second ed. Gulf Professional Publishing, Amsterdam. https://doi.org/10.1016/C2018-0-01643-6.

Blunt, M.J., Sun, S., Boone, M.A., et al., 2025. Digital rock physics and fluid flow in the context of the energy transition. Adv. Geo-Energy Res. 18 (3), 299–302. https://doi.org/10.46690/ager.2025.12.10.

Chen, H., Hu, Y., Kang, Y., et al., 2021a. Advantages of supercritical CO_2 compound fracturing in shale on fracture geometry, complexity and width. J. Nat. Gas Sci. Eng. 93 (4), 104033. https://doi.org/10.1016/j.jngse.2021.104033.

Chen, H., Hu, Y., Liu, J., et al., 2021b. Surface characteristics analysis of fractures induced by supercritical CO_2 and water through three-dimensional scanning and scanning electron micrography. J. Rock Mech. Geotech. Eng. 13 (5), 1047–1058. https://doi.org/10.1016/j.jrmge.2021.04.006.

Chen, J., Yang, R., Huang, Z., et al., 2023. Simulation study of supercritical carbon dioxide jet fracturing for carbonate geothermal reservoir based on fluid-thermo-mechanical coupling model. Pet. Sci. 20 (3), 1750–1767. https://doi.org/10.1016/j.petsci.2022.11.005.

Chen, K., Wu, F., Li, L., et al., 2024. Prioritizing organic pollutants for shale gas exploitation: life cycle environmental risk assessments in China and the US. Environ. Sci. Technol. 58 (19), 8149–8160. https://doi.org/10.1021/acs.est.3c10288.

Chen, L., Wang, S., Tao, W., 2019. A study on thermodynamic and transport properties of carbon dioxide using molecular dynamics simulation. Energy 179, 1094–1102. https://doi.org/10.1016/j.energy.2019.05.073.

Da, Q.A., Yao, C., Zhang, X., et al., 2024. Reservoir damage induced by water-based fracturing fluids in tight reservoirs: A review of formation mechanisms and treatment methods. Energy Fuels 38 (19), 18093–18115. https://doi.org/10.1021/acs.energyfuels.3c04963.

Dai, Q., Sun, W., Zuo, Y., et al., 2025. Impact of slickwater fracturing fluid on pore structure and micromechanical properties of clay-rich shale using fluid intrusion and AFM experiments. ACS Omega 10 (6), 6164–6181. https://doi.org/10.1021/acsomega.4c11005.

Gao, Y., Chen, W., Li, J., et al., 2022. Fracturing mechanism of granite by supercritical carbon dioxide under true triaxial stress. Geomech. Energy Environ. 32 (5), 100406. https://doi.org/10.1016/j.gete.2022.100406.

Gong, X., Ma, X., Liu, Y., et al., 2022. Advances in hydraulic fracture propagation research in shale reservoirs. Minerals 12 (11), 1438. https://doi.org/10.3390/min12111438.

Guo, R., Zhang, J., Zhao, P., et al., 2019. Accumulation conditions and an analysis of the origins of natural gas in the Lower Silurian Shiniulan Formation from well Anye 1, Northern Guizhou Province. Energies 12 (21), 4087. https://doi.org/10.3390/en12214087.

Guo, X., Liu, R., Xu, S., et al., 2022. Structural deformation of shale pores in the fold-thrust belt: the Wufeng-Longmaxi shale in the Anchang Syncline of Central Yangtze Block. Adv. Geo-Energy Res. 6 (6), 515–530. https://doi.org/10.46690/ager.2022.06.08.

Ha, S.J., Choo, J., Yun, T.S., 2018. Liquid CO_2 fracturing: Effect of fluid permeation on the breakdown pressure and cracking behavior. Rock Mech. Rock Eng. 51 (4), 3407–3420. https://doi.org/10.1007/s00603-018-1542-x.

Haikuan, N., Pei, L.I., Wei, D., et al., 2022. Enrichment characteristics and exploration directions of deep shale gas of Ordovician–Silurian in the Sichuan Basin and its surrounding areas, China. Petrol. Explor. Dev. 49 (4), 744–757. https://doi.org/10.1016/S1876-3804(22)60307-0.

Hazra, B., Vishal, V., Sethi, C., et al., 2022. Impact of supercritical CO_2 on shale reservoirs and its implication for CO_2 sequestration. Energy Fuels 36 (17), 9882–9903. https://doi.org/10.1021/acs.energyfuels.2c01894.

Hou, B., Zhang, R., Zeng, Y., et al., 2018. Analysis of hydraulic fracture initiation and propagation in deep shale formation with high horizontal stress difference. J. Pet. Sci. Eng. 170 (11), 231–243. https://doi.org/10.1016/j.petrol.2018.06.060.

Hou, Z., Yuan, Y., Chen, Y., et al., 2024. A review of supercritical CO_2 fracturing technology in shale gas reservoirs. Processes 12 (6), 1238. https://doi.org/10.3390/pr12061238.

Isaka, B.A., Ranjith, P.G., Rathnaweera, T.D., et al., 2019. Testing the frackability of granite using supercritical carbon dioxide: Insights into geothermal energy systems. J. CO2 Util. 34, 180–197. https://doi.org/10.1016/j.jcou.2019.06.009.

Lyu, Q., Tan, J., Li, L., et al., 2021. The role of supercritical carbon dioxide for recovery of shale gas and sequestration in gas shale reservoirs. Energy Environ. Sci. 14 (8), 4203–4227. https://doi.org/10.1039/D0EE03648J.

Meng, S., Jin, X., Tao, J., et al., 2021. Evolution characteristics of mechanical properties under supercritical carbon dioxide treatment in shale reservoirs. ACS Omega 6 (4), 2813–2823. https://doi.org/10.1021/acsomega.0c05136.

Ni, Y., Liu, S., Li, L., et al., 2024. Geochemical characteristics of shale gas hydraulic fracturing flowback/produced water in Zheng'an block, northern Guizhou Province, China. J. Nat. Gas Geosci. 9 (1), 27–37. https://doi.org/10.1016/j.jnggs.2024.01.001.

Pan, P., Wu, Z., Yan, F., et al., 2020. Effect of the intermediate principal stress on hydraulic fracturing in granite: An experimental study. Environ. Earth Sci. 79 (1), 10. https://doi.org/10.1007/s12665-019-8760-8.

Qianli, L., Bin, K., Jianchun, G., et al., 2025. Research on the mechanism of fracture propagation induced by shale hydration. Geosyst. Eng. 28 (5), 375–389. https://doi.org/10.1080/12269328.2025.2485113.

Qu, H., Li, Z., Li, C., et al., 2023. Experimental study of fracture initiation and morphology in low-brittle shales with bedding planes subjected to LN fracturing. Rock Mech. Rock Eng. 56 (6), 6299–6319. https://doi.org/10.1007/s00603-023-03407-y.

Qu, H., Tang, S., Liu, Y., et al., 2022. Characteristics of complex fractures by liquid nitrogen fracturing in brittle shales. Rock Mech. Rock Eng. 55 (1), 1807–1822. https://doi.org/10.1007/s00603-021-02767-7.

Rahimi-Aghdam, S., Chau, V., Lee, H., et al., 2019. Branching of hydraulic cracks enabling permeability of gas or oil shale with closed natural fractures. Proc Natl Acad Sci USA 116 (5), 1532–1537. https://doi.org/10.1073/pnas.1818529116.

Saberhosseini, S.E., Keshavarzi, R., Ahangari, K., 2014. A new geomechanical approach to investigate the role of in-situ stresses and pore pressure on hydraulic fracture pressure profile in vertical and horizontal oil wells. Geomech. Eng. 7 (3), 233–246. https://doi.org/10.12989/gae.2014.7.3.233.

Sun, W., Zuo, Y., Wang, S., et al., 2020. Pore structures of shale cores in different tectonic locations in the complex tectonic region: A case study of the Niutitang Formation in Northern Guizhou, Southwest China. J. Nat. Gas Sci. Eng. 80 (S1), 103398. https://doi.org/10.1016/j.jngse.2020.103398.

Sun, Y., Wang, X., Meng, Y., et al., 2025. Fracture propagation mechanism and application of supercritical CO_2 fracturing in shale: A review. Pet. Sci. 22 (4), 1625–1652. https://doi.org/10.1016/j.petsci.2025.01.009.

Wang, B., Jin, C.H., Liu, J., et al., 2025. Parameter optimization for multistage horizontal well fracturing based on multi-cluster perforation for deep coal measure gas: A case study of the Jurassic Baijiahai area in the Junggar Basin. Coal Geol. Explor. 53 (4), 86–93. https://doi.org/10.12363/issn.1001-1986.24.11.0746.

Wang, H., Chen, S., Zhang, S., et al., 2023. Study on fracture characteristics in coal and shale for coal-measure gas reservoir based on 3D CT reconstruction and fractal features. Front. Earth Sci. 17 (2), 514–526. https://doi.org/10.1007/s11707-022-1027-9.

Wu, F., Fan, X., Liu, J., et al., 2020. Analytical interpretation of hydraulic fracturing initiation pressure and breakdown pressure. J. Nat. Gas Sci. Eng. 76, 103185. https://doi.org/10.1016/j.jngse.2020.103185.

Wu, J., Huang, P., Maggi, F., et al., 2022. Molecular investigation on CO_2-CH_4 displacement and kerogen deformation in enhanced shale gas recovery. Fuel 315, 123208. https://doi.org/10.1016/j.fuel.2022.123208.

Wu, J., Tan, J., Xu, J., et al., 2025. Challenges to sustainable large-scale shale gas development in China. Proc Natl Acad Sci USA 122 (18), e1879775174. https://doi.org/10.1073/pnas.2415192122.

Wu, Z., Meng, X., Lan, B., et al., 2024a. Mechanical behavior of calcite vein-bearing shale of the Niutitang Formation in Fenggang area, northern Guizhou based on CT tests. Earth Sci. Front. 31 (5), 117–129 (in Chinese).

Wu, Z., Yang, C., Zuo, Y., et al., 2024b. Effect of natural fractures on mechanical properties and fracture patterns of shale at microscopic scale: an example from the Lower Cambrian Niutitang formation in Qianbei region. Geomech. Geophys. Geo-Energy Geo-Resour. 10 (1), 42. https://doi.org/10.1007/s40948-024-00743-3.

Xia, X., Wu, Z., Song, H., et al., 2024. Numerical study of hydraulic fracturing on single-hole shale under fluid–solid coupling. Geomech. Geophys. Geo-Energy Geo-Resour. 10 (1), 23. https://doi.org/10.1007/s40948-024-00746-0.

Yang, J., Lian, H., Li, L., 2020. Fracturing in coals with different fluids: An experimental comparison between water, liquid CO_2, and supercritical CO_2. Sci. Rep. 10 (1), 18681. https://doi.org/10.1038/s41598-020-75787-y.

Zhang, R., Wu, Z., He, G., et al., 2025. Study on the evolution characteristics of hydraulic fracturing cracks in shale with calcite veins under different horizontal stress differences. Arabian J. Sci. Eng. 1–21. https://doi.org/10.1007/s13369-025-10642-8.

Zhang, W., Hu, W., Borjigin, T., et al., 2020. Pore characteristics of different organic matter in black shale: A case study of the Wufeng-Longmaxi Formation in the Southeast Sichuan Basin, China. Mar. Petrol. Geol. 111, 33–43. https://doi.org/10.1016/j.marpetgeo.2019.08.010.

Zhang, X., Lu, Y., Tang, J., et al., 2017. Experimental study on fracture initiation and propagation in shale using supercritical carbon dioxide fracturing. Fuel 190, 370–378. https://doi.org/10.1016/j.fuel.2016.10.120.

Zhao, Z., Li, X., He, J., et al., 2018. A laboratory investigation of fracture propagation induced by supercritical carbon dioxide fracturing in continental shale with interbeds. J. Pet. Sci. Eng. 166 (7), 739–746. https://doi.org/10.1016/j.petrol.2018.03.066.

Zhou, H., Yan, T., Wang, B., et al., 2025a. Investigating rock properties and fracture propagation pattern during supercritical CO_2 pre-fracturing in conglomerate reservoir. Adv. Geo-Energy Res. 17 (2), 95–106. https://doi.org/10.46690/ager.2025.08.02.

Zhou, J., Wu, Z., Zuo, Y., et al., 2025b. Research on the prediction of permeability distribution characteristics of shale reservoirs based on current tectonic stress field: Case study of the Feng'gang Shale Gas Block III in the northern Guizhou area, China. Acta Geophys. 73 (1), 2269–2286. https://doi.org/10.1007/s11600-024-01519-9.

Zhou, Q., Xie, H.P., Zhu, Z.M., et al., 2023. Fracture toughness anisotropy in shale under deep in situ stress conditions. Rock Mech. Rock Eng. 56 (10), 7535–7555. https://doi.org/10.1007/s00603-023-03454-5.

Zhou, Y., Zhong, X., Nie, X., 2024. Identification and parameter characterization of pores and fractures in shales based on multi-scale digital core data. Adv. Geo-Energy Res. 13 (2), 146–160. https://doi.org/10.46690/ager.2024.08.08.